1   **Full-likelihood genomic analysis clarifies a complex history**
2   **of species divergence and introgression: the example of the**
3   ***erato-sara* group of *Heliconius* butterflies**

4   Yuttapong Thawornwattana[1], Fernando A. Seixas[1], Ziheng Yang[2*], James Mallet[1*]

5   [1] Department of Organismic and Evolutionary Biology, Harvard University, Cambridge, MA 02138,
6   USA

7   [2] Department of Genetics, Evolution and Environment, University College London, London WC1E
8   6BT, UK

9   **Corresponding authors**: z.yang@ucl.ac.uk, jmallet@oeb.harvard.edu

10

11   **Running head**: INTRODUCTION HISTORY OF ERATO-SARA HELICONIUS

12

13   ABSTRACT

14   Introgressive hybridization plays a key role in adaptive evolution and species diversification in many
15   groups of species. However, frequent hybridization and gene flow between species makes
16   estimation of the species phylogeny and key population parameters challenging. Here, we show
17   that by accounting for phasing and using full-likelihood analysis methods, introgression histories and
18   population parameters can be estimated reliably from whole-genome sequence data. We employ
19   full-likelihood methods under the multispecies coalescent (MSC) model with and without gene flow
20   to analyze the genomic data from six members of the *erato-sara* clade of *Heliconius* butterflies and
21   infer the species phylogeny and cross-species introgression events. The methods naturally
22   accommodate random fluctuations in genealogical history across the genome due to deep
23   coalescence. To avoid heterozygote phasing errors in haploid sequences commonly produced by
24   genome assembly methods, we process and compile unphased diploid sequence alignments and use
25   analytical methods to average over uncertainties in heterozygote phase resolution. There is robust
26   evidence for introgression across the genome, both among distantly related species deep in the
27   phylogeny and between sister species in shallow parts of the tree. We obtain chromosome-specific
28   estimates of key population parameters such as introgression directions, times and probabilities, as
29   well as species divergence times and population sizes for modern and ancestral species. We confirm
30   ancestral gene flow between the *sara* clade and an ancestral population of *H. telesiphe*, a likely
31   hybrid speciation origin for *H. hecalesia*, and gene flow between sister species *H. erato* and *H.*
32   *himera*. Inferred introgression among ancestral species also explains the history of two
33   chromosomal inversions deep in the phylogeny of the group. This study illustrates how a full-
34   likelihood approach based on the multispecies coalescent makes it possible to extract rich historical
35   information of species divergence and gene flow from genomic data.

36   **Keywords**: 3s, BPP, gene flow, *Heliconius*, introgression, multispecies coalescent, inversion, hybrid
37   speciation
38
39

40 INTRODUCTION

41 Thanks to increasing availability of genomic data and advances in analytical methods (Sousa and Hey
42 2013; Payseur and Rieseberg 2016), hybridization or introgression among species has been detected
43 in a variety of organisms, including *Anopheles* mosquitoes (Fontaine et al. 2015), *Panthera* cats
44 (Figueiró et al. 2017) and cichlid fishes (Malinsky et al. 2018), as well as *Heliconius* butterflies
45 (Dasmahapatra et al. 2012; Jay et al. 2018; Edelman et al. 2019; Kozak et al. 2021). Introgression is
46 increasingly recognized to be important in the transfer of genetic diversity across species, and it
47 likely contributes to adaptive evolution (Mallet et al. 2016; Taylor and Larson 2019; Edelman and
48 Mallet 2021). Understanding gene flow and the role it plays during divergence is today seen as
49 important for a fuller understanding of speciation (Pinho and Hey 2010; Feder et al. 2012).

50 A common approach for inferring the species phylogeny from genomic data has been to estimate
51 phylogenetic trees based on concatenated genomic data. However, gene flow and other factors can
52 lead to phylogenetic discordance within whole genome data. Given a species phylogeny, summary
53 methods such as the *D* statistic (or ABBA-BABA test) (Patterson et al. 2012) are then often used to
54 detect cross-species gene flow. This whole-genome test for gene flow is useful, but it ignores
55 information in the local variation of the gene tree across the genome, and is unable to infer gene
56 flow between sister species or the direction and timings of gene flow between non-sister species.
57 More recently, phylogenetic analysis of sliding windows across the genome have been used to
58 investigate the causes for phylogenetic discordance, particularly introgression. Sliding-
59 window/concatenation analysis is a useful descriptive tool for exploratory analysis of genomic data
60 (Martin and Van Belleghem 2017), but it could run into difficulties when used in inference. The
61 assumption of a single gene tree for the whole sliding window (which may have a size of 10kb or
62 100kb) may be unrealistic. Furthermore, the proportions of gene trees among the sliding windows
63 may not have a simple biological interpretation. Even under a model of complete isolation, large
64 fluctuations in gene tree topology and branch lengths are expected due to natural coalescent
65 fluctuations (Barton 2006): the probability that the (true) gene tree has a different topology from the
66 species tree can range anywhere from near 0% to near 100%, depending on the parameters in the
67 model. Estimated gene trees are affected by phylogenetic errors which are known to inflate the
68 gene-tree discordance (Yang 2002). Introgression adds further variation. Furthermore, proportions
69 of estimated gene trees from sliding windows are sensitive to the window size: with small windows,
70 the results may be affected by phylogenetic errors, whereas with large windows, one or two gene
71 trees will dominate due to the averaging effects, even though the average gene tree for the sliding
72 window may differ from the species tree (Roch and Steel 2015). Thus it may not be straightforward
73 to use the proportions of gene tree topologies from sliding windows to infer the presence of gene
74 flow or to estimate its strength. For example, a previous sliding-window phylogenomic analysis of
75 the *Anopheles gambiae* group of African mosquitoes appears to have produced an incorrect
76 backbone species tree (Fontaine et al. 2015), as a coalescent-based re-analysis suggested a different
77 species tree that is more consistent with chromosomal inversions and with known patterns of gene
78 flow among the species (Thawornwattana et al. 2018).

79 Another common issue is the treatment of heterozygous sites in unphased diploid sequence data. A
80 standard practice in genome assembly has been to "haploidify" the diploid sequence to a single
81 haploid sequence for each genome, with each heterozygous site represented by only one nucleotide
82 base, e.g., the one with more reads. This loses half of the information, and, worse still, produces
83 chimeric haplotypes that do not exist in nature because the genotypic phase of multiple
84 heterozygous sites is resolved effectively at random. Recent simulation studies (Andermann et al.
85 2019; Huang et al. 2021) found that such haploid consensus sequences can lead to serious biases in
86 downstream phylogenomic analyses if the species tree is shallow, with species divergence times
87 comparable to coalescent times. The impact of phasing errors in haploidified sequences on
88 estimation of species trees and inference of gene flow is poorly understood. The BPP program (Yang

89   2015; Flouri et al. 2018) implements the algorithm of Gronau et al. (2011), which enumerates and
90   averages over all possible phase resolutions of heterozygote sites, weighting them according to their
91   likelihood based on the sequence alignment at the locus. In simulations, this approach performed
92   nearly as well as analysis of fully phased diploid genomes (which could be generated, for instance, by
93   costly single-molecule cloning and sequencing) (Huang et al. 2021).

94   Here, we test coalescent-based full-likelihood phylogenomic approaches that explicitly account for
95   deep coalescence and introgression as sources of genealogical variation across the genome while
96   accounting for unphased diploid sequences probabilistically. One approach is based on a
97   multispecies coalescent model with introgression (MSci) (Wen and Nakhleh 2018; Zhang et al. 2018),
98   implemented in the program BPP (Flouri et al., 2020). In this approach, introgression is modelled as
99   discrete events that occur at particular time points in the past. Another approach is based on an
100 isolation-with-migration (IM) model (Hey and Nielsen 2004; Hey 2010) implemented in the program
101 3s (Zhu and Yang 2012; Dalquen et al. 2017), which allows for continuous migration at a constant
102 rate per generation between two species after their divergence. Advantages of full-likelihood
103 methods over approximate coalescent methods or summary statistics include making full use of
104 information in the sequence data and properly accounting for uncertainty in gene trees (Xu and Yang
105 2016; Jiao et al. 2021). These methods allow us not only to infer the presence of gene flow, but also
106 to estimate its direction, timing and magnitude, along with species divergence times and effective
107 population sizes. Estimation of these key evolutionary parameters from genome-scale sequence
108 data can provide powerful insights into the divergence history of species, and a basis for further
109 investigations of the evolution of adaptive traits of interest.

110 We use *Heliconius* butterflies as a trial group to explore the power of these methods. *Heliconius* is a
111 rapidly radiating group in tropical America (Kozak et al. 2015). They are unpalatable to predators
112 and are perhaps best known for mimicry, which causes multiple unrelated sympatric species to
113 converge on similar wing patterns in local regions as a common warning sign to deter predators
114 (Bates 1862; Müller 1879). The genus *Heliconius* comprises two major clades, the *erato-sara* clade
115 and the *melpomene*-silvaniform clade, which diverged around 10–12 million years ago (Ma) in the
116 Miocene (Kozak et al. 2015). Natural hybridization among species is well-documented within each
117 clade (Mallet et al. 2007). The prevalence of introgression between species coupled with rapid
118 radiation of species makes estimation of the species phylogeny challenging (Kozak et al. 2021). As a
119 result, our understanding of the history of species divergence and introgression in *Heliconius*
120 remains incomplete. Here, we estimate the species phylogeny and introgression history of six
121 species in the *erato-sara* clade of *Heliconius* butterflies from whole-genome sequence data.

122 Most previous studies of the genus *Heliconius*, including the *erato* group, have focused on
123 evolutionary relationships and gene flow at specific regions of the genome, especially the colour
124 pattern loci responsible for phenotypic variation in the mimetic wing patterns, typically in a few
125 species, and mainly in the *melpomene*-silvaniform clade where gene flow appears to be more
126 prevalent (Dasmahapatra et al. 2012; Nadeau et al. 2013; Martin and Van Belleghem 2017; Jay et al.
127 2018; Balaban et al. 2019). Other studies have focused on wing-colour mimicry loci between two
128 species with comimic races, *H. erato* (*erato-sara* clade) and *H. melpomene* (*melpomene*-silvaniform
129 clade) (Hines et al. 2011; Reed et al. 2011).

130 Earlier molecular phylogenetic studies of *Heliconius* were based on a small number of loci (Brower
131 1994; Brower and Egan 1997; Beltrán et al. 2002; Beltrán et al. 2007; Kozak et al. 2015), revealing
132 variation in gene genealogies among loci. In particular, Kozak et al. (2015) employed BUCKy (Larget
133 et al. 2010) and *BEAST (Heled and Drummond 2010) to account for the heterogeneity of gene
134 genealogies across loci. Hybridization and introgression were acknowledged but not directly
135 accounted for in the analysis. Kozak et al. (2021) analyzed genome-wide coding loci from >100
136 individuals from 40 *Heliconius* species to estimate the species tree using approximate multispecies
137 coalescent (MSC) methods such as ASTRAL (Mirarab et al. 2014) and MP-EST (Liu et al. 2010), and to

138   test for introgression using a range of summary methods including the D statistic (or ABBA-BABA
139   test) (Patterson et al. 2012), f_4 (Reich et al. 2009), and an approximate multispecies coalescent with
140   introgression (MSci) method PHYLONET/MPL (Yu and Nakhleh 2015). However, D and f_4 statistics use
141   site-pattern counts averaged over the genome, ignoring information in genealogical fluctuations,
142   while PHYLONET/MPL takes estimated gene trees as input without accounting for phylogenetic
143   reconstruction errors and uncertainties. Van Belleghem et al. (2017) estimated the species
144   phylogeny of the *erato* clade from concatenated autosomal SNP data, focusing on wing colour
145   pattern loci among different geographic races of *H. erato*.

146   Recently, Edelman et al. (2019) conducted phylogenetic analyses with sixteen new genome
147   assemblies of *Heliconius* species using ASTRAL to analyze gene trees and from sliding windows
148   (Mirarab et al. 2014). Introgression was tested using D statistics (Patterson et al. 2012) and a new
149   test called QuIBL based on internal branch lengths in estimated triplet gene trees. Summary
150   methods such as D statistics are based on genome-wide averages and ignore information from
151   genealogical variation across the genome in multilocus sequence data. QuIBL may be affected by
152   sampling errors in estimated gene trees and branch lengths. Those methods typically cannot infer
153   gene flow between sister species and have limited ability to characterize the direction, timing, and
154   magnitude of gene flow (as measured by the migration rate or introgression probability) between
155   non-sister species. In Edelman et al. (2019), MSci network models were inferred using
156   PHYLONET/MCMC_SEQ (Wen and Nakhleh 2018), a Bayesian Markov chain Monte Carlo (MCMC)
157   method based on sequence alignments. However, the method is computationally applicable only to
158   a small number of loci, leading to considerable uncertainty of species tree topology and timing and
159   directions of introgression (Edelman et al. 2019). Finally, Massardo et al. (2020) re-analyzed genome
160   data from the *erato-sara* clade after adding two additional genomes using approaches similar to
161   those of Edelman et al. (2019). Given known limitations of concatenation, the sliding-windows, and
162   summary methods, we hypothesized that our methodology could add additional resolution using the
163   genomic data employed by Edelman et al. (2019).

164   In this paper, we processed the raw reads for the genomic data of Edelman et al. (2019) for six
165   species in the *erato-sara* clade to compile alignments of unphased diploid genomic sequences, and
166   used them as input data for analysis using BPP.

167

168   METHODS

169   *Genome sequence data and genotyping*

170   We used the raw sequencing read data from six *Heliconius* species in the *erato-sara* clade and *H.*
171   *melpomene* (as an outgroup) generated by Edelman et al. (2019) (**Table S1**). Sequencing reads were
172   filtered for Illumina adapters using cutadapt v1.8.1 (Martin, 2011) and then mapped to the
173   chromosome-level genome assembly of *H. erato demophoon* v1 (Van Belleghem et al. 2017)
174   available from lepbase.org, using BWA mem v0.7.15 (Li 2013) with default parameters and marking
175   short split hits as secondary. Mapped reads were sorted and duplicate reads removed using
176   sambamba v0.6.8 (Tarasov et al. 2015). Realignment around indels was performed with the Genome
177   Analysis Toolkit (GATK) v3.8 *RealignerTargetCreator* and *IndelRealigner* modules (McKenna et al.
178   2010; DePristo et al. 2011) in order to reduce the number of indel miscalls. Read depth and other
179   relevant read alignment quality control metrics were computed using QualiMap v2.2.1
180   (Okonechnikov et al. 2016).

181   Genotype calling was performed on each individual separately with bcftools v1.5 (Li et al. 2009)
182   *mpileup* and *call* modules (Li 2011), using the multiallelic-caller model (*call -m*) and requiring a
183   minimum base and mapping quality of 20. Genotype calls were filtered using the bcftools *filter*
184   module. Both invariant and variant sites were required to have a minimum quality score (QUAL) of

185 20. Furthermore, we required that each genotype had a genotype quality score (GQ) ≥20 and a read
186 depth (DP) satisfying max(1/2*meanDP, 20) ≤ DP ≤ 2*meanDP where meanDP is the average read
187 depth of the sample. The meanDP-based filters were used to reduce erroneous calls when the read
188 depths were too low or too high from the sample average, accounting for variation of sequencing
189 depths across individuals. The DP ≥ 20 filter was chosen to minimize genotyping error rates (see next
190 section) while retaining a sufficiently large number of loci across the genome. At our estimated
191 base-calling error (~0.1%), this filter achieved the genotype-calling error of <0.05% (see next section)
192 (**Fig. 1**, **Tables S2–S3**). For the female Z chromosome, we used DP ≥ 10 instead since only one
193 chromosome copy was present. All genotypes that did not fulfill these requirements or were located
194 within 5-bp of an indel were recoded as missing data.

195
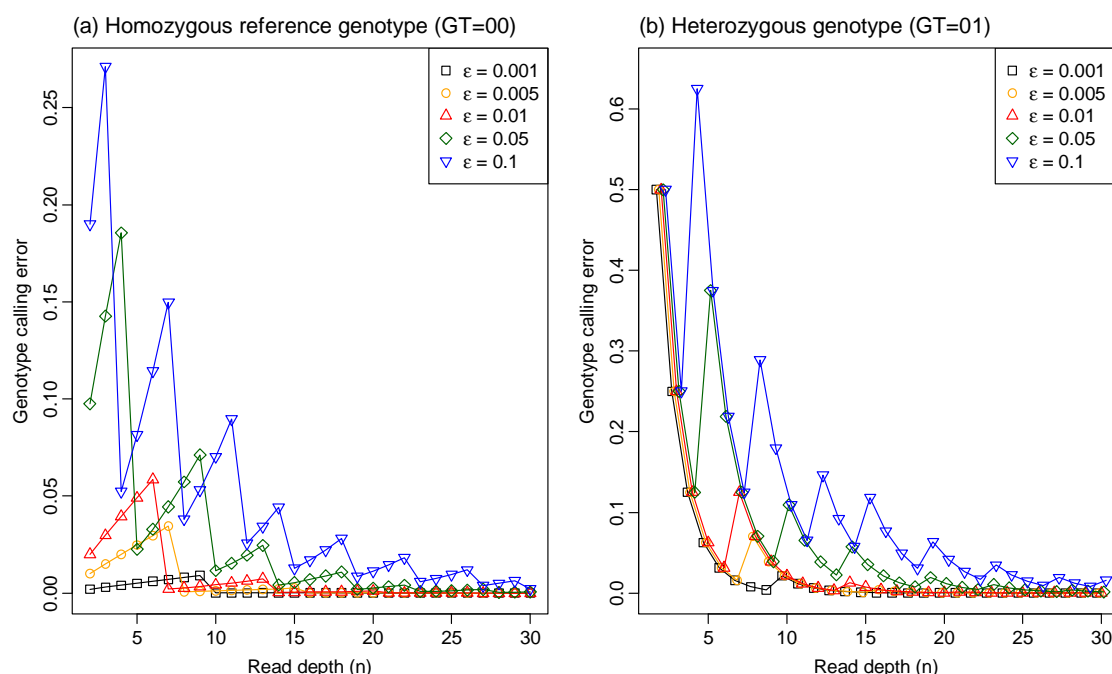
196 **Figure 1**. The genotype-calling error rate for a given base-calling error (ε) and read depth (n) when
197 the true genotype is (**a**) a homozygote for the reference allele (GT = 00) or (**b**) a heterozygote (GT =
198 01). Note that the genotype-calling error does not decrease monotonically with the increase in n
199 when ε is fixed, or with the reduction in ε when n is fixed. The calculation is performed using a C
200 program written by Z.Y. that implements the ML method of Li (2011) and calculates its error rate.

201

202 *Analysis of base-calling and genotype-calling error rates to guide data compilation*

203 The base-calling error rate was estimated from the proportion of non-matching bases in
204 homozygous genotype calls from reads mapped to the *H. melpomene* reference genome, which was
205 more complete than the *H. erato demophoon* reference. Only positions with homozygous genotype
206 calls with read depth (DP) ≥ 50 were retained. Because mapping errors can bias our estimates of
207 base-calling error rate, sites overlapping repetitive regions were excluded. For sites passing those
208 filters, we recorded the read depth (DP) and the number of reads supporting each of the reported
209 alleles (AD), with the difference to be the number of erroneous base calls. The base-calling error
210 was calculated as the ratio of the number of erroneous base calls over the read depth, both summed
211 across all sites passing filters. The calculation was done for homozygous reference genotype (GT =
212 00) and homozygous alternative genotype (GT = 11).

213 We then analyzed the genotype-calling error rate to determine a suitable cutoff for the read depth,
214 following the maximum likelihood (ML) method for genotype-calling of Li (2011). The results were
215 used to guide our choice of the filter (DP ≥ 20), to achieve a genotype-calling error of <0.05%.

216 Given the base-calling error rate (ε) and the read depth (n), the genotype-calling error rate (e) can be
217 calculated by following the ML procedure of genotype calling of Li (2011). Here we assume that ε is
218 the same among the reads and is independent of the true base. Given the data of k 1s and ($n - k$) 0s
219 among the n reads, where 0 refers to the reference allele and 1 refers to the alternative allele, the
220 likelihoods for the three genotypes (GT = 00, 01, and 11) are given by the binomial probabilities as

$$L(00|k) = \Pr(k|\text{GT}=00) = \binom{n}{k}(1-\varepsilon)^{n-k}\varepsilon^k,$$

221 $$L(01|k) = \Pr(k|\text{GT}=01) = \binom{n}{k}\left(\tfrac{1}{2}\right)^n, \tag{1}$$

$$L(11|k) = \Pr(k|\text{GT}=11) = \binom{n}{k}(1-\varepsilon)^k\varepsilon^{n-k}$$

222 (Li 2011). The genotype achieving the highest likelihood is the called (inferred) genotype. The
223 genotype-calling error is an average over the possible read outcomes (i.e., over $k = 0, ..., n$)

224 $$e_{\text{GT}=00} = \sum_{k=0}^{n}\Pr(k|\text{GT}=00)\times I_{GT\neq00}, \tag{2}$$

$$e_{\text{GT}=01} = \sum_{k=0}^{n}\Pr(k|\text{GT}=01)\times I_{GT\neq01},$$

225 where the indicator $I_{GT\neq00}$ is 1 if the called genotype (from data k) is not 00 (in error) and 0
226 otherwise, and $I_{GT\neq01}$ is defined similarly.

227

Multilocus datasets for BPP and 3s analyses

229 We prepared two sets of data, one for BPP analyses (under the MSC and MSci models) and the other
230 for 3s analysis (under the IM model). The 'BPP dataset' has six species in the *erato-sara* clade. The
231 '3s dataset' has an extra species, *H. melpomene*, as an outgroup (**Table S1**) (Edelman et al. 2019).
232 Both datasets were prepared in the same way. For each dataset, we defined coding and noncoding
233 regions based on the gene annotation of *H. erato demophoon* v1 reference assembly (Van
234 Belleghem et al. 2017), where coding regions included exons while noncoding regions included
235 introns and intergenic regions. For the noncoding regions, we extracted the genotype calls for small
236 genomic segments, referred to as loci, with sizes between 100 and 2,000 bp, and with the further
237 requirement that any two consecutive loci must be at least 2,000 bp apart. Although linkage
238 disequilibria largely disappear over ~10 kb (Dasmahapatra et al. 2012), we used this minimum
239 distance of 2 kb to retain more information in the data for species tree estimation. For each locus,
240 we produced sequence alignments from the genotype calls, with heterozygotes represented using
241 IUPAC codes. We applied the following filtering steps: (1) Sites within repetitive regions (based on
242 the repeat annotation of *H. erato demophoon* v1 reference assembly, available at
243 http://download.lepbase.org/v4/repeatmasker/) were masked; (2) loci with >50% missing data in
244 the whole alignment were excluded; (3) for the remaining loci, sites with missing data were
245 excluded; (4) finally, loci with ≤10 sites remaining after processing were excluded. For the coding
246 regions, the same filtering process was applied except that there was no maximum locus size. There
247 were 74,999 coding loci (median length of 165 and median informative sites of 3) and 92,966
248 noncoding loci (median length of 237, median number of informative sites of 5).

249

Inferring species divergence history across the genome using multispecies coalescent model

251   We inferred species trees using Bayesian inference under the MSC model without gene flow
252   implemented in BPP v4.3.0 (Yang and Rannala 2014; Rannala and Yang 2017; Flouri et al. 2018). This
253   analysis under the MSC accounts for deep coalescence and the resulting gene tree heterogeneity
254   along the genome but assumes no gene flow. We analyzed autosomes and the Z chromosome
255   separately and coding and noncoding regions of autosomes separately. Two inversion regions in
256   chromosomes 2 and 15 were analyzed separately, denoted 2b and 15b, respectively. The 2b region
257   included part of the Herato0211 scaffold (from position 1434133) and the whole scaffolds
258   Herato0212, Herato0213 and Herato0215 (a total of 1.95 Mb). The 15b region corresponded to
259   Herato1505:1977997–2558395 (580 kb), which included the *cortex* gene (Herato1505:2074108–
260   2087841, ~13.7 kb). Thus, there were 25 chromosomal regions in total (for 21 chromosomes, with
261   chromosomes 2 and 15 split into three regions).

262   For each of the datasets (coding and non-coding loci from the Z chromosome and autosomes), we
263   formed multilocus blocks of 100 loci and inferred the species tree for the block (**Table S4**). This block
264   size was large enough for the inferred species tree to achieve reasonably high posterior support and
265   yet small enough to allow for local introgression history to be reflected in the inferred 'species tree'
266   for that region. Any final blocks for each chromosomal region with fewer than 40 loci were
267   discarded due to limited information. To assess the impact of block size, we repeated the analysis
268   using blocks of 200 loci. While the neutral coalescent process may be expected to be largely
269   homogeneous across the genome, the introgression rate is expected to be highly variable, due to
270   selective removal of introgressed alleles, affected by the strength of selection, local recombination
271   rate, etc. The analysis using blocks of loci can thus capture the variation across the genome due to
272   differential rates of gene flow. Note that both our block-based analysis and the sliding-windows
273   analysis of Edelman et al. (2019) may capture the variation in the rate of gene flow across the
274   genome, but there is an important difference. The 100 or 200 loci in the same block are assumed to
275   have independent genealogical histories due to coalescent fluctuations even though they have the
276   same underlying species tree. In the sliding-windows/concatenation analysis, all sites in the whole
277   sliding window are assumed to share the same gene tree and divergence times. In other words, the
278   block-based analysis assumes no recombination within each locus (100-2000 bp) while the sliding-
279   windows analysis assumes no recombination in the window of 10kb or 50kb.

280   The MSC model involves two sets of parameters: the species divergence times or node ages on the
281   species tree (τ) and the effective population sizes ($\theta = 4N\mu$). Both are scaled by mutations and
282   measured in the expected number of substitutions per site. We assigned diffuse inverse-gamma
283   priors to those parameters, with a shape parameter of 3 and with the means to be close to rough
284   estimates from the data in preliminary runs. Specifically, we used $\theta \sim$ InvG(3, 0.04), with mean
285    $0.04/(3 - 1) = 0.02$ for all populations, the root age $\tau_0 \sim$ InvG(3, 0.06) for the coding loci and $\tau_0 \sim$
286   InvG(3, 0.12) for the noncoding loci. Given τ_0, divergence times at other nodes of the species tree
287   were generated from a uniform-Dirichlet distribution (Yang and Rannala 2010, eq. 2). Population-
288   size parameters (θ) are integrated out analytically to improve mixing of the MCMC.

289   The MCMC was run for 2×10^6 iterations after a burn-in of 10^5 iterations, with samples taken every 20
290   iterations. The same analysis of each block was repeated ten times using different starting species
291   trees, and consistency among runs was used to assess convergence of the MCMC. Non-convergent
292   runs were discarded. Samples were then combined to produce the posterior summary such as the
293   maximum a posteriori (MAP) tree.

294

295   *Exploring gene flow scenarios using the IM model for species triplets*

296   In order to formulate hypotheses about gene flow between species, we attempted to use several
297   heuristic methods, including PHYLONET/MCMC_SEQ using sequences (Wen and Nakhleh 2018),
298   PHYLONET/ML (Yu et al. 2014), and SNaQ in PHYLONETworks (Solís-Lemus et al. 2017), the latter two
299   using estimated gene trees as input data. Our attempts were not successful. Different runs of those
300   programs inferred different network models, which in general did not appear to be reliable, with
301   apparently spurious introgression events around the root of the species tree.

302   Instead we decided to use the maximum likelihood program 3S (Dalquen et al. 2017) to estimate
303   migration rates between all pairs of species. This implements the IM model with continuous gene
304   flow for three species S_1, S_2 and S_3, assuming the species tree $((S_1, S_2), S_3)$, with gene flow allowed
305   only between S_1 and S_2. The third species (S_3) is used as an outgroup to improve parameter
306   estimation and the power of the test (Dalquen et al. 2017). This method accommodates both deep
307   coalescence and gene flow. While limited to three species and three sequences per locus, it can be
308   applied to large datasets with >10,000 loci. *H. melpomene* was used as an outgroup for all pairs.
309   The outgroup species was added to the dataset by mapping it to the *H. erato demophoon* reference
310   genome.

311   We analyzed coding and noncoding regions, as well as the autosomal loci and the Z chromosome
312   separately. However, in the 3S analysis we treated all loci in each chromosomal region as one
313   dataset (rather than breaking them into blocks of 100 or 200 loci) (**Table S4**). We also performed an
314   analysis that used all autosomal loci (17,428 noncoding or 28,204 coding loci; **Table S4**). Since the
315   sequences were unphased and 3S requires phased haploid sequences, we first phased the loci using
316   PHASE v2.1.1 (Stephens et al. 2001), resulting in two phased haploid sequences for each locus per
317   individual. In the simulations of Huang et al. (2021), which examined the Bayesian method BPP, this
318   approach of computational phasing produced very small biases, and the same may be expected to
319   apply to the ML method implemented in 3S. The 3S program uses three sequences but allows
320   multiple sequences per species. For each locus, we sampled three sequences of configurations 123,
321   113 and 223 with probabilities 0.5, 0.25 and 0.25, respectively. Here, 123 means one sequence from
322   each species, etc.

323   Each dataset was analyzed using 3S to fit two models: MSC without migration (M0) and MSC with
324   migration (M2; isolation-with-migration or IM). Model M0 involves two divergence time parameters
325   (τ_1 and τ_0) and four effective population sizes (θ_1 and θ_2 for species S_1 and S_2, θ_4 for the root, and θ_5
326   for the ancestor of S_1 and S_2), while M2 involves in addition two migration rates in both directions
327   M_{12} and M_{21}. Here $M_{12} = m_{12}N_2$ is the expected number of migrants from species S_1 to S_2 per
328   generation, where m_{12} is the proportion of migrants from S_1 in species S_2. We use the real-world
329   forward-in-time view to define migration parameters. Each ML analysis was repeated ten times, and
330   the run with the highest log-likelihood value was used. The two models (M0 and M2) were
331   compared using a likelihood ratio test (LRT), with χ_2^2 used as the null distribution. Only gene flow
332   scenarios that passed the LRT at the 1% level were considered later.

333   Evidence for pairwise gene flow from the 3S analysis was used together with the inferred species
334   trees from the blockwise BPP MSC analysis to generate an MSci model or a species tree with
335   introgression events. There were two difficulties in this approach. First, IM (3S) and MSci (BPP) are
336   two extreme versions of models of gene flow and either may be too simplistic to fit the real data.
337   The IM model assumes continuous gene flow between species S_1 and S_2 since their split, and may be
338   unrealistic for many of the species pairs, for example, if gene flow occurred immediately after
339   species split but then stopped as the two species became more diverged. This is particularly the
340   case as a branch in the 3-species tree used in the 3S analysis may represent multiple branches in the
341   full tree for all six species. The MSci model instead assumes episodic introgression events at specific
342   time points. Our expectation is that if introgression is episodic, the LRT based on the continuous IM

343   model will still detect gene flow, but with distorted parameter estimates. The opposite may be true
344   as well: if gene flow is continuous as in the IM model, fitting the MSci model will give distorted
345   parameter estimates (Jiao et al. 2020). Second, the LRT suggested significant evidence for gene flow
346   between most pairs of species. We prioritized introgression events that could reconcile different
347   species trees across the genome from the above blockwise BPP analysis under the MSC model. We
348   also took a parsimonious approach to minimize the number of introgression events by assuming
349   gene flow only if the model of no gene flow is rejected by data: if 3s suggested gene flow between a
350   species A and most descendant species of a node B, we assumed introgression edges between the
351   ancestral populations.

352

353   *Estimation of parameters for species divergence and cross-species introgression*

354   Given the MSci model constructed above, we ran BPP v4.3.0 (Flouri et al. 2020) to estimate the
355   parameters: species divergence/introgression times (τ), population sizes (θ), and introgression
356   probabilities (φ). The introgression probability is the proportion of contribution from the parental
357   species to the hybridizing population. When we trace the genealogy of a sampled sequences
358   backwards in time and reach a hybridization node, the sequence takes the paths of the two parental
359   species with probabilities φ and $1 - \varphi$, respectively. We assigned $\theta \sim$ InvG(3, 0.01), with mean 0.005,
360    $\tau_0 \sim$ InvG(3, 0.04) and $\varphi \sim$ beta(4, 2), with mean 0.75. Initial values of φ were set to 0.8 or 0.9. These
361   prior settings were based on rough estimates from preliminary runs. We also considered alternative
362   priors for θ (e.g. gamma distributions) and φ (e.g. beta(1,1)) to assess the stability of the posterior
363   estimates when mixing and convergence were of concern. We performed inference for each of the
364   25 chromosomal regions, using either all coding or noncoding loci in each region (**Table S4**).

365   The MCMC was run for 10^6 iterations, sampling every 100 iterations, after a burn-in of 10^6 iterations.
366   Ten independent runs were performed and convergence was assessed by examining consistency
367   between runs. Non-convergent runs were discarded. For models with bidirectional introgressions
368   (BDIs) which cause label-switching unidentifiability issues (Flouri et al. 2020), MCMC samples were
369   post-processed before being combined for posterior summaries.

370

371   RESULTS

372   *Analysis of base-calling and genotype-calling error rates*

373   We processed the raw reads from the whole-genome sequence data of Edelman et al. (2019) for six
374   *Heliconius* species from the *erato-sara* clade: *H. erato demophoon*, *H. himera*, *H. hecalesia formosus*,
375   *H. telesiphe telesiphe*, *H. demeter* and *H. sara magdalena* (**Table S1**). To guide our compilation of
376   unphased loci, we estimated the base-calling error rate in the genomic data and analyzed the
377   genotype-calling error. The base-calling error was calculated to be ~0.08% for the homozygous
378   reference allele and ~0.20% for the homozygous alternative allele, with variation among individual
379   genomes (**Tables S2–S3**).

380   Given a base-calling error rate (ε), we calculated the genotype-calling error rate (e) for the
381   homozygous reference genotype (GT = 00) and the heterozygous genotype (GT = 01) by using
382   equation (2) (**Fig. 1**). Note that even with a very low base-calling error rate, the genotype-calling
383   error can be very high, especially at low read depth. Furthermore, the genotype-calling error rate
384   for heterozygotes is much higher than for homozygotes.

385   Given the read depth n, the genotype-calling error does not necessarily decrease when ε decreases.
386   For example, when n = 7, the genotype-calling error for a homozygote (GT = 00) is 0.0020 at ε = 0.01,

387   but rises to 0.0345 when ε is reduced to 0.005 (**Fig. 1**). This is due to the discrete nature of the read
388   outcome. At $\varepsilon = 0.01$, the called genotype is 00 (the truth) when $k = 0$ or 1, is 01 when $k = 2$–5 and is
389   11 when $k = 6$ or 7, and the genotype-calling error is a sum over $k = 2, ..., 7$ (i.e., six out of the eight
390   cases are in error). In contrast, at $\varepsilon = 0.005$, the called genotype is 00 when $k = 0$, is 01 when $k = 1$–6
391   and is 11 when $k = 7$, so that the genotype-calling error is a sum over $k = 1, ..., 7$ (i.e., seven out of
392   the eight cases are in error), and is higher than at $\varepsilon = 0.01$. Similarly given ε, the genotype-calling
393   error does not necessarily decrease with the increase of the read depth n (**Fig. 1**). For example,
394   when $\varepsilon = 0.01$ the genotype-calling error for a homozygote is 0.0199 at $n = 2$, but rises to 0.0585
395   when n increases from 2 to 6; for those values of n, genotype-calling error is a sum over $k = 1, ..., n$.
396   Then when $n = 7$, error drops to 0.00269 as the error is a sum over $k = 2, ..., n$. These anomalies and
397   the strong periodicity in the genotype-calling error are both due to the discrete nature of the
398   problem.

399   With the base-calling error estimated at $\varepsilon \approx 0.001$, we estimate the genotype-calling error rate to be
400   1.1×10^{-6} for homozygotes and 4.0×10^{-4} for heterozygotes at the read depth $n = 20$ (**Fig. 1**). We
401   therefore filtered our data for coverage $n \geq 20$. Since the read coverage was >60x (Edelman et al.
402   2019), this caused relatively little dropout.

403

404   *Gene flow variation across the genome*

405   We first used BPP to infer species trees under the MSC model using multilocus blocks of 100 or 200
406   independent loci along the genome. There were 749 coding blocks and 933 noncoding blocks over
407   the 25 chromosomal regions (21 chromosomes with chromosomes 2 and 15 each split into three
408   regions by inversion) (**Table S4**). This is the BPP A01 analysis of Yang (2015), which explicitly accounts
409   for deep coalescence but ignores gene flow. Ten species trees were the best estimate (i.e., the
410   maximum *a posteriori* probability tree or MAP tree) in at least one block (**Fig. 2**, **Tables S5–S7**).
411   These are referred to as trees i-x. Tree xi appeared as one of the top eight trees in the sliding-
412   window analysis of Edelman et al. (2019) but not in our analysis. Trees i and ii accounted for over
413   95% of the blocks. These two trees differ only in the position of *H. hecalesia* within the *erato* clade:
414   in tree i, *H. hecalesia* is sister to *H. telesiphe* while in tree ii, it is sister to the clade (*H. erato, H.*
415   *himera*).

416   The species trees estimated in this analysis are expected to reflect the history of species divergences
417   as well as cross-species introgression, and the major cause of the differences among the blocks is the
418   variable rate of introgression along the genome. The use of 100 or 200 loci in each block helps to
419   filter out local stochastic fluctuations in the coalescent process. The results were highly consistent
420   between the two choices of block size and between coding and noncoding loci (**Fig. 2**), providing
421   evidence that the patterns revealed are real rather than a result of analytical artefacts.

422
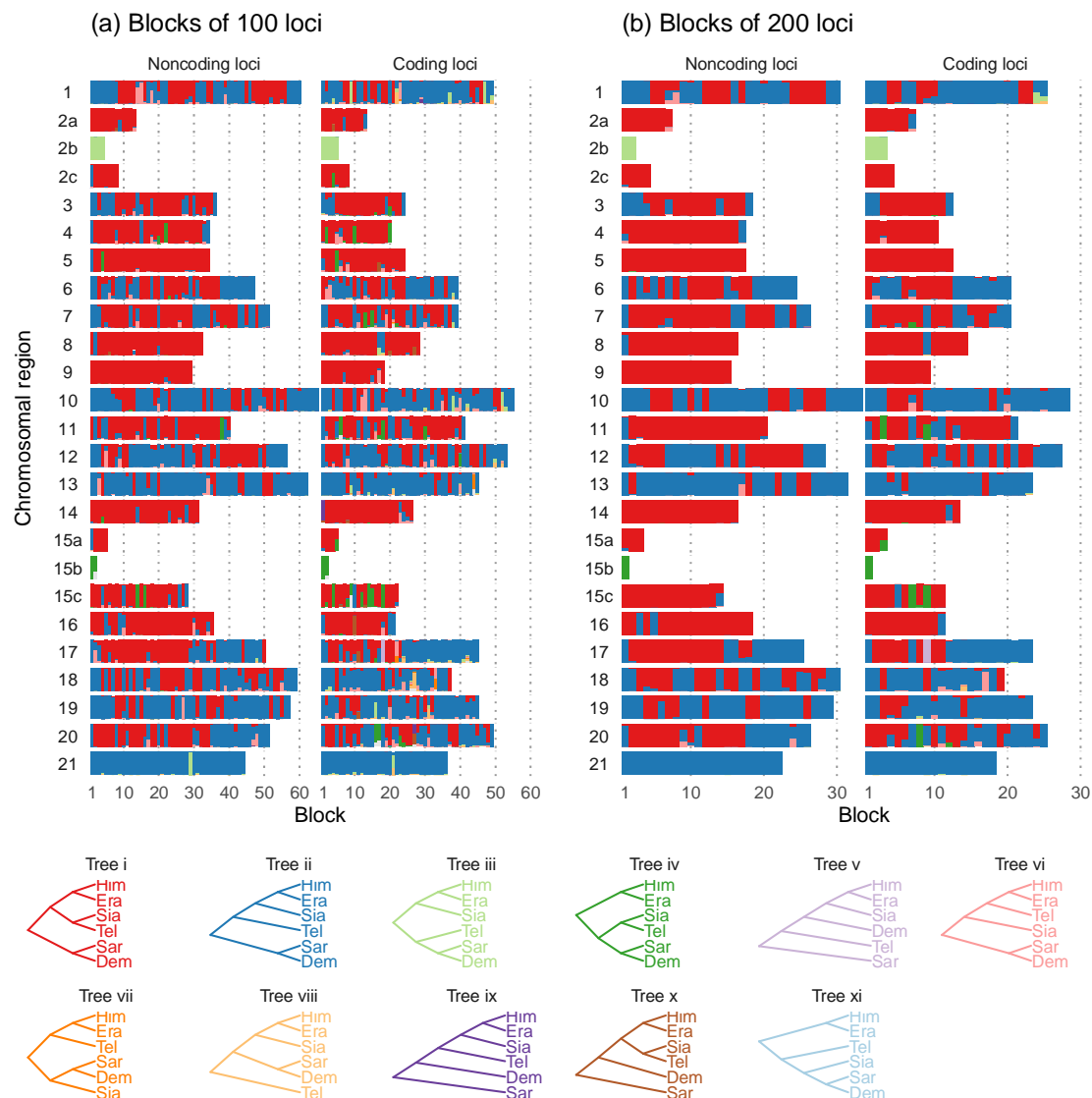
Figure 2. Posterior probabilities of species trees from BPP analysis of (**a**) blocks of 100 loci and (**b**) blocks of 200 loci across the genome (**Table S4**) under the MSC model without gene flow. The y-axis represents the posterior probability and ranges from 0 to 1. Trees i–x in the legend are MAP trees in at least one block. Tree colours match those in Edelman et al. (2019) (their Fig. 2). Inversion regions 2b and 15b on chromosomes 2 and 15 were analyzed separately. Era: *H. erato*, Him: *H. himera*, Sia: *H. hecalesia*, Tel: *H. telesiphe*, Dem: *H. demeter*, Sar: *H. sara*.

There was some variation in the estimated species trees across the genomic regions. Three regions in particular had species tree distributions that differed from the rest of the genome: chromosome 21 (Z chromosome), and the inversions on chromosomes 2 and 15 (2b and 15b). Chromosome 21 was the only chromosome for which tree ii is a MAP tree for almost all blocks (**Fig. 2**, **Table S5**). Among the autosomal regions excluding inversions, tree ii was the MAP tree in ~40% and 46% of noncoding and coding blocks, respectively, while the corresponding proportions for tree i were 58% and 47% (**Table S5**). Thus, tree i was the autosomal majority tree. Inversion 2b had an unusual history in which *H. telesiphe* is more closely related to the *sara* clade (tree iii). In this inversion region, *H. erato*, *H. himera* and *H. hecalesia* share a derived inverted rearrangement relative to *H.*

440   *melpomene, H. sara* and *H. demeter* (Van Belleghem et al. 2017; Davey et al. 2017; Edelman et al.
441   2019), consistent with trees ii and iii where these species are clustered together. Inversion 15b
442   supported tree iv in both coding and noncoding regions, in which the (*H. telesiphe, H. hecalesia*)
443   clade was sister to the *sara* clade instead of other members of the *erato* clade as in tree i or ii. This
444   grouping strongly suggests that *H. telesiphe, H. hecalesia, H. demeter* and *H. sara* share the derived
445   inverted rearrangement of this region relative to *H. erato* (Edelman et al. 2019). The 15b inversion
446   contains the *cortex* gene that controls mimetic wing colour patterning across *Heliconius* species
447   (Nadeau et al. 2016; Van Belleghem et al. 2017). Tree iv also appeared as a MAP tree sporadically in
448   other parts of the autosomes, sometimes with high posterior probabilities (**Fig. 2**, **Table S6**). These
449   include regions on chromosome 15 outside the inversion as well as on chromosomes 4, 5 and 11.

450

451   *Pairwise gene flow rates*

452   Gene flow among species could reconcile different species trees from the blockwise BPP MSC
453   analysis reported above. We investigated this by explicitly estimating gene flow rates between
454   each pair of *erato-sara* group species using the program 3s (Zhu and Yang 2012; Dalquen et al.
455   2017). We used *H. melpomene* as an outgroup in all triplets for parameter estimation.

456   There was evidence of bidirectional gene flow between *H. telesiphe* and *H. hecalesia*, consistent
457   with a scenario in which tree i (autosome-majority tree) and tree ii (Z chromosome tree) are
458   related through introgression between the two species (**Fig. 3**). However, gene flow between
459   these species was detected only for autosomal loci (both coding and noncoding) and not on the Z
460   chromosome (**Fig. 3**). The results suggest that the prevailing topology on the Z chromosome, tree
461   ii rather than tree i, is the true species tree. In particular, we found no evidence of gene flow in
462   3s analyses from *H. erato* and *H. himera* towards *H. hecalesia* (**Fig. 3**), which is necessary to
463   explain tree ii as a result of introgression if tree i were the true species tree.

464   Given tree ii, the Z chromosome (in particular the noncoding loci) was almost devoid of gene
465   flow, in sharp contrast with the autosomes (**Fig. 3**, **Table S8**). For the autosomes, the highest
466   rates of migration according to 3s were between the two sister species *H. erato* and *H. himera*,
467   with gene flow occurring in both directions (at the rate of 0.085–0.121 migrants per generation
468   from *H. himera* to *H. erato* and 0.048–0.067 in the opposite direction) (**Fig. 3**). There was gene
469   flow into *H. erato, H. himera* and *H. demeter* from every other species, and from *H. sara* to all
470   other species. These results were largely consistent among the individual autosomes (**Fig. S1**),
471   across pairs of species (**Fig. S2**).

472   The pattern of gene flow inferred using 3s may reflect complex introgression in this group of
473   species as well as the difficulty of using pairwise migration rates to reconstruct the full migration
474   history for all species. If gene flow involved ancestral branches on the tree for all six species, we
475   would expect the LRT to detect it in multiple pairs of species, although with distorted estimates of
476   times and rates of migration. One scenario is extensive introgression involving common
477   ancestors of the *sara* group and the *erato* group, which should show up as initial gene flow after
478   species divergence that ceased after a certain time.

479   We used the results from the previous two analyses, blockwise BPP and 3s, to formulate a
480   plausible history of species divergences and cross-species introgression for the *erato-sara* clade.
481   The Z chromosome tree from the BPP analysis was used as the backbone, onto which 3s-
482   supported introgression events were added to reconcile other species trees from the blockwise
483   BPP analysis (**Fig. 4a**).

484
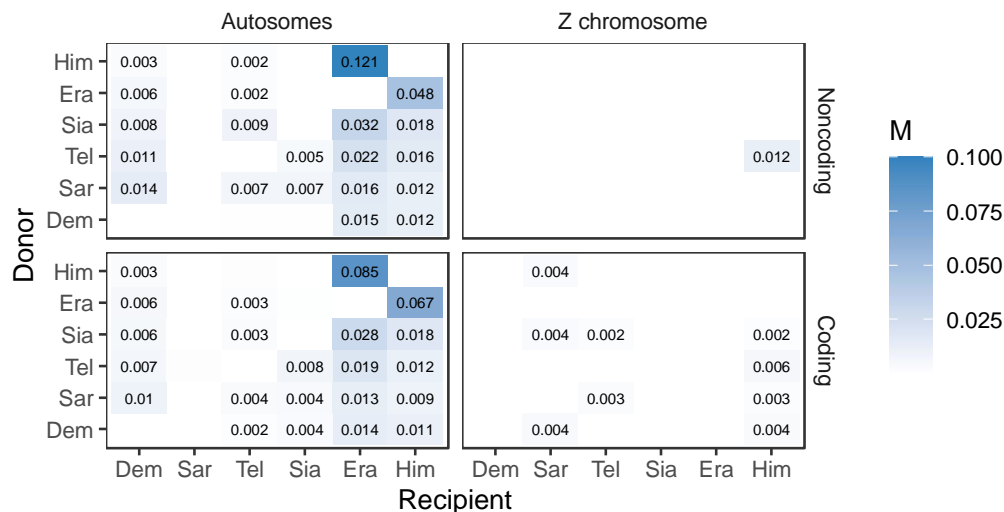
Figure 3. Maximum-likelihood estimates of the migration rates ($M = Nm$) under the IM model from 3s using all 28,204 coding and 17,428 noncoding loci in the autosomes (left column) and 1,348 coding and 574 noncoding loci in the Z chromosome (right column) for each pair of species. The donor and recipient species of gene flow are given in the y- and x-axis, respectively. *H. melpomene* was used as an outgroup. Only significant migration rate estimates (by likelihood ratio test at $p < 0.01$) larger than 0.001 are shown. See **Figure S2** and **Table S8** for estimates of other parameters.
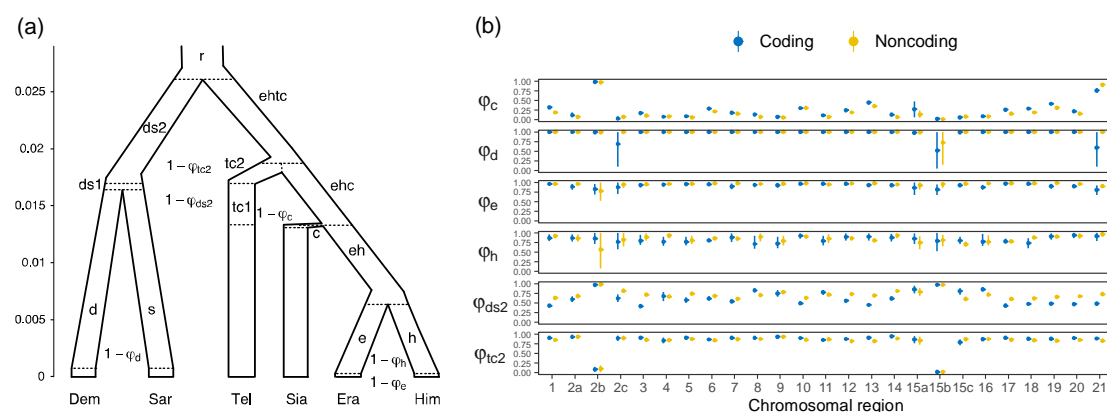
Figure 4. (**a**) The introgression (MSci) model, proposed based on the BPP species tree estimation under MSC and 3s analysis under the IM model, involving two unidirectional introgression events (s → d with introgression probability $1 - \varphi_d$, and tc1 → c with probability $1 - \varphi_c$) and two bidirectional introgression (BDI) events (e ↔ h with probabilities $1 - \varphi_e$ and $1 - \varphi_h$, and ds2 ↔ tc2 with probabilities $1 - \varphi_{ds2}$ and $1 - \varphi_{tc2}$). The model involves 34 parameters: 5 species divergence times and 4 introgression times (τs), 19 population sizes (θs), and 6 introgression probabilities. To identify parameters (see **Fig. S3**), internal nodes are labelled with lowercase letters, e.g., e is the parent node of Era, eh is the parent node of e and h, etc. Each branch corresponds to a population and is referred to using the label for its daughter node, e.g., branch e-Era is labelled branch Era and has population size θ_{Era}, and branch eh-e is labelled branch e and has θ_e. Branch lengths in the tree represent posterior means of divergence/introgression times in the BPP analysis of the 6,030 noncoding loci in chromosome 1. Estimates for other chromosomes or for coding loci are presented

507   in **Figure 5**. (**b**) Posterior means (dots) and 95% HPD intervals (bars) of the six introgression
508   probabilities $(1 - \varphi)$ under the MSci model of (**a**) obtained from BPP analysis of the 25 chromosomal
509   regions (see **Table S4** for the number of loci). Estimates for other parameters are in **Figure S3**.
510   Inversion regions 2b and 15b on chromosomes 2 and 15 were analyzed separately, and there was an
511   alternative set of posterior estimates resulting from within-model unidentifiability; see **Figure 6**.

512

513   *Construction of a full history of species divergences and cross-species introgression*

514   We then used the MSci model or species tree with introgressions of **Figure 4a** to estimate the
515   introgression probabilities $(1 - \varphi)$ as well as species divergence/introgression times (τ) and
516   population size parameters (θ) for each chromosomal region. (Note: in the version of BPP used here,
517    $1 - \varphi$ is the introgression probability for the horizontal branch representing introgression, while
518   more recent versions from 4.4.0 onwards use φ instead). All coding loci are analyzed as one dataset
519   for each chromosomal region, as are all noncoding loci. These correspond to the A00 analysis under
520   MSci in BPP (Flouri et al. 2020).

521   Estimates of introgression probability from *H. telesiphe* into *H. hecalesia* were consistently high $(1 - $
522    $\varphi_c > 0.5$, ~0.8 on average) across the genome, except for the 2b inversion region and Z chromosome
523   (**Figs. 4b, 5**). The time estimates suggest that this introgression occurred almost immediately after
524   *H. hecalesia* split from the common ancestor of *H. erato* and *H. himera* (**Fig. 5**), supporting the
525   hypothesis that *H. hecalesia* is a hybrid species generated during a single catastrophic event. Even
526   though our model assumed different times for species divergence (τ_{ehc}) and for introgression (τ_c),
527   with $\tau_{ehc} > \tau_c$ (equivalent to model B in Flouri et al. (2020)), posterior estimates strongly suggest that
528   those two times actually coincided, with $\tau_{ehc} \approx \tau_c$ (equivalent to model C in Flouri et al. (2020)). This
529   pattern was consistent with our estimates of the species trees from blockwise BPP analysis (**Fig. 2**)
530   where the autosomes, except for the 2b region, were dominated by tree i as a result of *H. telesiphe*
531    $\rightarrow$ *H. hecalesia* introgression on tree ii.

532   For the more ancient introgression between *H. telesiphe* and the common ancestor of *H. demeter*
533   and *H. sara*, the estimated introgression probability from *H. telesiphe* $(1 - \varphi_{ds2})$ was substantial
534   across the entire genome, ~0.3–0.4 on average, with $1 - \varphi_{tc2} \approx 0.1$ in the reverse direction (**Fig. 4b**,
535   **Table S9**). This suggests genome-wide flow between the *erato* clade and the *sara* clade prior to the
536   *H. telesiphe* $\rightarrow$ *H. hecalesia* introgression/hybridization. The estimates of $1 - \varphi_{ds2}$ and $1 - \varphi_{tc2}$ in the
537   two small inversion regions, 2b and 15b, were more extreme, very close to either 0 or 1, with
538   complex identifiability issues. We discuss the introgression history of the two inversion regions
539   below.

540   Other introgression events had relatively low probabilities across the genome despite evidence from
541   the 3s analysis under the IM model. Introgression between *H. erato* and *H. himera* had probabilities
542   of $1 - \varphi_h \approx 15\%$ for *H. erato* $\rightarrow$ *H. himera* and $1 - \varphi_e \approx 5\%$ for *H. himera* $\rightarrow$ *H. erato*, consistently
543   throughout the genome (**Fig. 4b**). Note that the introgression probability in the MSci model is
544   expressed as the proportion of immigrants in the receiving population at the time of hybridization,
545   so the smaller rate in the *H. himera* $\rightarrow$ *H. erato* direction may reflect the large population size for *H.*
546   *erato*. In contrast, the migration rate in the IM model is estimated to be in the range of 0.07–0.12
547   migrants per generation, and is larger in the *H. himera* $\rightarrow$ *H. erato* direction (**Fig. 3**). These gene flow
548   estimates also vary considerably among chromosomes (**Figs. S1–S2**, **Table S8**).

549   Lastly, our BPP MSci analysis did not support the *H. sara* $\rightarrow$ *H. demeter* introgression suggested by 3s
550   analysis. The introgression probability $(1 - \varphi_d)$ was either small (<1%) or had a large posterior
551   interval in all chromosomal regions (**Fig. 4b**), neither of which provided strong support for such
552   introgression.

553 Overall, estimates of species divergence/introgression times (τ) and population sizes (θ) were
554 broadly consistent across chromosomal regions as well as between coding and noncoding loci, with
555 sufficient numbers of loci to yield estimates with high precision (**Fig. S3**, **Table S9**). In particular,
556 estimates of divergence times were highly similar among chromosomal regions and were nearly
557 perfectly proportional between coding and noncoding loci, with the regression $\tau_C \approx 0.6\tau_{NC}$ ($r^2 \geq 0.99$)
558 (**Fig. S4**). The slope suggests that purifying selection on coding loci reduced the neutral mutation
559 rate to about 0.6 × that of noncoding loci. While the noncoding and coding regions of the genome
560 have drastically different functions, when used as markers in the BPP analyses they yield highly
561 consistent estimates concerning the history of species divergences and cross-species introgression.
562 This consistency indicates that the results are reliable. Similarly, the estimates of population sizes
563 were nearly proportional between coding and noncoding loci, with the regression $\theta_C \approx 0.6\,\theta_{NC}$ ($r^2 \geq$
564 0.9) (**Fig. S5**). Background selection may be expected to reduce within-species polymorphism (θ) via
565 linked selection but not between-species divergence (τ) (Shi and Yang 2018). The near identical
566 regression slopes for both τ and θ suggest a limited role of background selection in reducing neutral
567 sequence variation.

568 The age of the base of the *erato-sara* clade (τ_r) was estimated to be about 0.027 substitutions per
569 site for noncoding loci on average (**Fig. S3**, **Table S9**). If we use the mutation rate of 2.9×10^{-9}
570 neutral mutations per site per generation and 4 generations per year (Keightley et al. 2015), this
571 translates to about 2.3 million years (Ma) of divergence.

572 Population size parameters (θ) for populations corresponding to short branches on the species tree
573 (**Fig. 4a**) were difficult to estimate reliably, with considerable variation among chromosomes and
574 large posterior intervals (**Fig. S3**, **Table S9**), reflecting both low information content and the impact
575 of the heavy-tailed inverse gamma prior. Most populations had θ in the order of 0.01 while a few
576 had more extreme estimates. *H. erato* (θ_{Era}) had small values, in the order of 0.0001–0.001, for most
577 chromosomes, except in the 2b inversion where the θ_{Era} estimates were unreliable due to lack of
578 data. In the current implementation of the MSci model, the same species before and after an
579 introgression event are considered distinct species and are assigned independent θ parameters. It
580 appears more sensible to assign the same θ, in particular when the introgression event is inferred to
581 be nonexistent (as in the case of the *H. sara* → *H. demeter* introgression) and/or to be extremely
582 recent. Thus we believe the estimates of θ for the parent populations prior to introgression events
583 are more appropriate estimates for the four modern species: *H. demeter* ($\theta_d \approx 0.01$, better than θ_{Dem}
584 $\approx 0.002\text{-}0.004$), *H. sara* ($\theta_s \approx 0.01$, better than $\theta_{Sar} \approx 0.06\text{-}0.13$), *H. erato* ($\theta_e \approx 0.06\text{-}0.30$, better than
585 $\theta_{Era} \approx 0.0001\text{-}0.0166$) and *H. himera* ($\theta_h \approx 0.005\text{-}0.017$, better than $\theta_{Him} \approx 0.0009\text{-}0.0022$) all for
586 noncoding autosomal loci (**Table S9**). The genome sequences of *H. erato* and *H. himera* were
587 obtained from partially inbred individuals to aid assembly, which likely explains their apparent low
588 effective population sizes and large variation among chromosomes. The *H. erato* genome, in
589 particular, has long stretches of homozygosity on some chromosomes due to inbreeding (**Fig. S6**)
590 corresponding approximately to per-chromosome estimates of θ_{Era}.

591

(a) Noncoding loci

(b) Coding loci

592
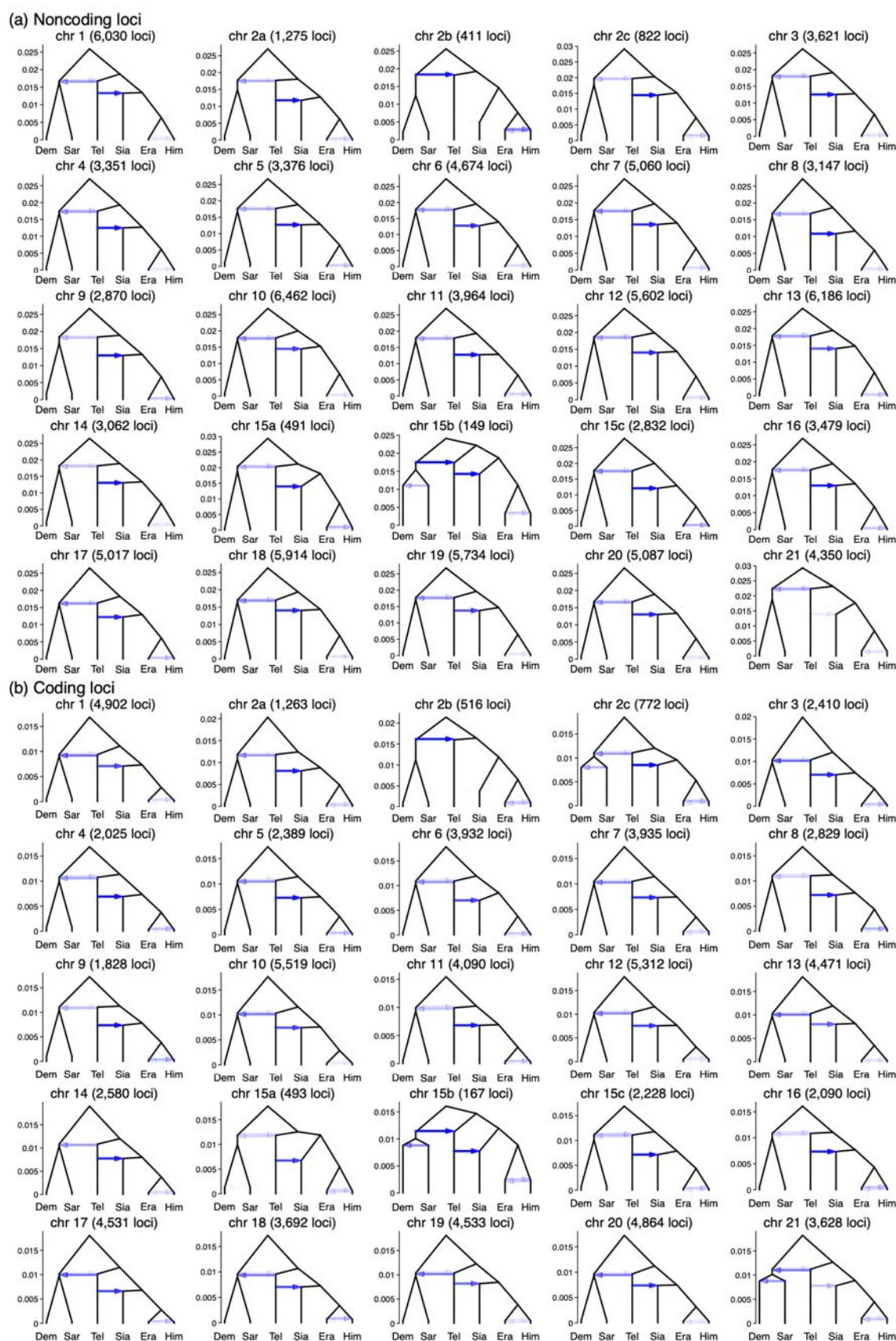
593 **Figure 5**. Estimated introgression history in each chromosomal region obtained from bpp analysis
594 under the MSci model (**Fig. 4a**) using (**a**) noncoding and (**b**) coding loci. Intensity of the horizontal
595 edges represents the posterior means of the six introgression probabilities (see **Fig. 4b**), while the y-
596 axis represents the nine divergence/introgression times in the expected number of mutations per
597 site. A full list of posterior estimates and 95% HPD intervals, including nineteen population size
598 parameters, is in **Table S9**.

599

600 DISCUSSION

601 *Major features of the species tree and introgression: comparison with previous studies*

602 In this study, we processed genomic sequence data from the *erato-sara* clade of *Heliconius* from
603 Edelman et al. (2019) and compiled unphased diploid sequence alignments. We assessed the
604 probable genotype calling error rate based on our high coverage reads and used a high coverage
605 filter to exclude almost all genotype calling errors. We then used the data to infer the history of
606 speciation and introgression under the MSci model in a full-likelihood framework, accounting for
607 unphased diploid genomic data probabilistically without collapsing heterozygous sites. This
608 coalescent-based full-likelihood method is an improvement over summary methods or sliding-
609 window/concatenation analysis, which make less efficient use of information from genomic
610 sequence data.

611 In general, our analysis confirms several major conclusions from previous analyses but reveals
612 improved details of the evolutionary history for the clade. As in Edelman et al. (2019), we find that
613 the Z chromosome supports tree ii, while autosomes favour tree i. We weigh the evidence and find
614 that the Z chromosomal tree is almost certainly the true species tree (see 'Pairwise gene flow rates'),
615 even though large-scale introgression has distorted genealogical histories of autosomes so that the
616 most common gene tree in the genome has a different topology (mostly tree i). Such major
617 genealogical conflicts between the sex chromosome and the autosomes were inferred also in other
618 species groups including *Anopheles gambiae* (Fontaine et al. 2015; Thawornwattana et al. 2018),
619 felids (Li et al. 2019) and small finches (Stryjewski and Sorenson 2017). In the *Anopheles gambiae*
620 group of African mosquitoes, the X chromosomal tree was similarly inferred to be the species tree
621 while the autosomal tree reflects rampant gene flow (Fontaine et al. 2015; Thawornwattana et al.
622 2018). However, sliding-window analysis of genomic data from the *Anopheles gambiae* group
623 (Fontaine et al. 2015) led to an incorrect species tree; coalescent-based full-likelihood methods
624 produced a tree more consistent with chromosomal inversion data and with established patterns of
625 cross-species hybridization and gene flow (Thawornwattana et al. 2018). In the *Heliconius* dataset,
626 in contrast, concatenated windows and MSci analyses yield similar species trees. Concatenation may
627 produce anomalous gene trees (Roch and Steel 2015) so that the estimated gene trees from large
628 sliding windows may differ from the species phylogeny, but this was not the case for the *Heliconius*
629 data. In the *Anopheles gambiae* group, all species arose very rapidly, creating very short internodes
630 at the base of the species tree, while the six *Heliconius* species studied here are well separated with
631 longer internal branches (**Fig. 4a**). Thus, the sliding-window gene tree approach was more successful
632 in *Heliconius* than in the *Anopheles gambiae* group.

633 We also tested the impact of phasing errors, by generating datasets with heterozygote phase
634 resolved at random for chromosome 1, to mimic the haploid consensus sequences. From the
635 blockwise BPP MSC analysis (30 noncoding and 25 coding 200-locus blocks), we found that phasing
636 errors had little impact on species tree estimation, with random phasing producing identical or
637 highly similar posterior probabilities and the same MAP species tree. However, phasing errors had
638 greater impact on estimation of parameters under the MSci model of **Figure 4a**: the divergence
639 times and modern population sizes tend to be overestimated (**Fig. S7**, using all 4,902 coding loci and

640   6,030 noncoding loci from chromosome 1). These results are consistent with simulations, where
641   species tree estimation was more robust and parameter estimation was more sensitive to phasing
642   errors (Huang et al. 2021).

643   Our improved data processing and the use of full-likelihood approach also made it possible to
644   answer additional questions. For example, D statistics and internal branch length tests (Edelman et
645   al. 2019) can be used to test for the presence of gene flow, but cannot identify gene flow between
646   sister species, infer the direction of gene flow or estimate its magnitude between non-sister species.
647   In contrast, migration rates and introgression probabilities in the IM and MSci models, which
648   measure the magnitude of gene flow, can be estimated from genomic data using full likelihood
649   methods (Jiao et al. 2021). The proportions of gene trees in sliding-window/concatenation analyses
650   are sensitive to the window size and are not directly comparable with introgression probabilities or
651   even with proportions of species trees in the blockwise BPP MSC analysis.

652   For example, the frequencies of estimated gene trees i and ii in Edelman et al. (2019) are 24.3% and
653   25.8% among 10kb sliding windows (their Fig. S78), but are 35.5% and 34.8% among the 50kb
654   windows (mapped to the *H. erato* reference, their Fig. 2B), and 36.4% and 45.4% among the 50 kb
655   windows (mapped to the more distant *H. melpomene* reference, their Fig. S77). The proportion of
656   windows with the dominant gene tree will increase when the window becomes larger due to the
657   averaging effect of concatenation. In our blockwise BPP MSC analysis, local variation in the rate of
658   gene flow among species (affected by linkage to selected loci and local recombination rate) is
659   expected to be the most important factor leading to fluctuations among blocks, as gene-tree
660   conflicts due to ancestral polymorphism are filtered out by the MSC model. In the BPP MSC analysis,
661   the frequencies of (species) trees i and ii are 54.8% and 42.8% among the 100-loci noncoding blocks,
662   44.2% and 48.3% among the 100-loci coding blocks, 58.9% and 40.2% among the 200-loci noncoding
663   blocks, and 46.9% and 49.5% among the 200-loci coding blocks. These are reasonably consistent
664   between coding and noncoding loci and seem less sensitive to the number of loci in each block than
665   is the sliding-window analysis to the window size.

666   There was a greater representation of the presumed introgression tree i in noncoding loci (55-59%)
667   than in coding loci (44-47%) compared with tree ii, and a moderate excess of *H. telesiphe* → *H.*
668   *hecalesia* introgression $(1 - \varphi_c)$ in noncoding versus coding loci on each chromosome (**Fig. 4b**). This
669   may reflect greater constraint on introgression for coding sequences as found in other systems, for
670   instance for Neanderthal ancestry in modern humans (Sankararaman et al. 2014).

671   Previous estimates of migration rates and timings in *Heliconius* under models of gene flow such as
672   the IM model have been limited to a few loci (Bull et al. 2006; Kronforst et al. 2006; Kronforst 2008;
673   Salazar et al. 2008; Pardo-Diaz et al. 2012) or a few species (Kronforst et al. 2013; Van Belleghem et
674   al. 2021), most of which have focused on the *melpomene* clade. Using joint site-frequency spectrum
675   and a secondary contact model, Van Belleghem et al. (2021) estimated migration rates ($M = Nm$) to
676   be around 0.5–0.6 migrants per generation from two races of *H. erato* (*H. erato favorinus* and *H.*
677   *erato emma*) to *H. himera*, and 0.07–0.13 in the opposite direction. This asymmetric gene flow
678   accords with our MSci results, in which the probability of flow is 15% from *H. erato* to *H. himera*, and
679   5% in the opposite direction (**Fig. 4b**, **Table S9**). Our estimates from the 3s analysis of the genomic
680   data are 0.05–0.07 migrants per generation from *H. erato* to *H. himera*, and 0.09–0.12 in the
681   opposite direction. The differences may be due to different data and methods used. No estimates
682   of other introgression probabilities in **Fig. 4** have previously been reported.

683

684   *Limitations of our analyses*

685   Implementation of the MSci model in BPP (Flouri et al. 2020) provides a powerful tool for estimating
686   the timing and magnitude of introgression on a species phylogeny from genome-scale data while

687   accounting for deep coalescence and genealogical heterogeneity across the genome. The
688   implementation also retains heterozygous sites in the genomic data and averages over all possible
689   heterozygote phase resolutions (Gronau et al. 2011), avoiding systematic errors caused by the use of
690   haploid consensus sequences (Huang et al. 2021). Other likelihood-based methods incorporating
691   cross-species gene flow are under active development (Hey et al. 2018; Wen and Nakhleh 2018;
692   Zhang et al. 2018; Jones 2019), but they are computationally demanding and currently impractical
693   for data of >100 loci. We have also tested for the effects of sequencing error on genotype calls;
694   erroneous genotype calls may also potentially obscure the genealogical signal in the data. We find
695   that genotype call error in our data should be very low due to high read coverage (>20x after
696   processing).

697   Here we discuss several limitations of our approach. First, the introgression model we formulated
698   (**Fig. 4a**) relies on two main sources of information: variation in the species tree estimated from
699   blocks of loci across the genome and pairwise migration rate estimates from 3s. Integrating such
700   information into a single MSci model is non-trivial. Ideally, we would be able to infer the species
701   phylogeny and introgression events simultaneously with associated parameters such as
702   introgression and divergence times, but this has yet to be implemented.

703   Second, even with a fixed MSci model (**Fig. 4a**), inference of demographic parameters is
704   computationally challenging. Some parameters were difficult to estimate reliably, such as
705   population sizes associated with short branches in the species tree (e.g., θ_{Sar} and θ_{ds1}; see **Fig. S3**).
706   Contributing factors include unidentifiability of the model, multimodal posterior distribution, poor
707   MCMC mixing, and potential model misspecification. The unidentifiability arises because of the
708   symmetry in the likelihood induced by bidirectional introgression (BDI, such as the two BDI events in
709   the model of **Figure 4a**) (Flouri et al. 2020). The BDI between nodes ds2-tc2 (**Fig. 4a**) is between
710   non-sister species and creates a pair of unidentifiable models (**Fig. S8**). The BDI at nodes e-h (**Fig. 4a**)
711   is between sister-species and leads to a pair of unidentifiable likelihood peaks within the same
712   model (not shown). We prefer species tree S_1 of **Figure S8** because the introgression probabilities
713   are $1 - \varphi_{ds2} < \frac{1}{2}$ and $1 - \varphi_{tc2} \approx 0.1$, while the alternative model S_2 has introgression probabilities $\varphi_{ds2} >$
714    $\frac{1}{2}$ and $\varphi_{tc2} \approx 0.9$, implying mutual replacements of the species involved; this does not seem plausible
715   biologically. Similarly for the BDI event at e-h, we focus on the peak with small introgression
716   probabilities (with $1 - \varphi_e < \frac{1}{2}$ and $1 - \varphi_h < \frac{1}{2}$) (**Fig. 4b**). In other words, we resolve the
717   unidentifiability caused by BDI events by applying simple constraints such as $1 - \varphi < \frac{1}{2}$, as
718   recommended by Flouri et al. (2020). An example of MCMC outputs and processing is provided in
719   **Figure S9**. Furthermore, unidentifiability can occur when the introgression probability is estimated
720   to be 0 or 1. This is the case for the 2b and 15b inversions; see our discussions of the different
721   inversion introgression scenarios below.

722   Third, we avoid explicit modeling of recombination by analyzing short genomic loci (~200 bp on
723   average) that are far apart (at least 2 kb). This assumes that sites within each locus have zero
724   recombination, whereas different loci are free to recombine. Sites are expected to be approximately
725   independent at physical distances of ~10 kb apart, at least based on linkage disequilibrium decay
726   estimated from the *H. melpomene* group species (Dasmahapatra et al. 2012, their Fig. S16.2.1).
727   Thus, some correlation of gene genealogies between consecutive loci may be expected. The
728   unrealistic assumption of free recombination between loci is expected to have a slight effect of
729   exaggerating information content within each block of loci, leading potentially to artificially narrow
730   credibility intervals for parameter estimates. The assumption of no recombination among sites of
731   the same locus may be of more concern since recombination causes different parts of the sequence
732   to have different histories while the model assumes one history. However, the loci used in this study
733   are so short that the assumption of no recombination within a locus is expected to hold
734   approximately. Previously, Lanier and Knowles (2012) found that species tree estimation under MSC
735   is robust to realistic levels of recombination. The impact of recombination on estimates of the

736   migration rate or introgression probability is not well understood, in particular when recombination
737   rate varies across the genome.

738   Fourth, the migration (IM) models in 3s and the MSci model in BPP are necessarily simplified.
739   Currently we lack a good understanding of the behaviour of our inference methods when the model
740   of gene flow is misspecified, for example, when the MSci model is fitted to data generated under the
741   IM model or vice versa (Jiao et al. 2020, Fig. 7). One may expect the magnitude of gene flow to vary
742   across the genome and over time. We are currently investigating the performance of estimation
743   methods such as 3s and BPP under such complex scenarios of gene flow, in order to develop methods
744   that account for such variation.

745

746   *Introgression history of the two inversion regions*

747   Our analyses consistently suggest that two inversion regions, 2b and 15b, have genetic histories
748   distinct from the rest of the genome (**Figs. 4b, 5**). All introgression probabilities for those two
749   regions were close to either 0 or 1, except for estimates which involve large uncertainties due to lack
750   of data. This suggests that loci within each of the two inversion regions were inherited almost
751   without recombination as a single locus. This is likely if an inverted region introgresses and becomes
752   fixed in a population that previously lacked the inversion (or vice-versa), and if, during the period of
753   polymorphism, recombination in the inverted region was strongly suppressed – a known biological
754   effect of inversions. Although the MSC framework explicitly models ancestral polymorphism,
755   inversion polymorphism is not accounted for since it creates substructure within the ancestral
756   population while the model assumes random mating within species and free recombination among
757   loci. Nonetheless, introgression probabilities of either 0 or 1 are sensible estimates. When
758   introgression probabilities are near 0 or 1, some parameters can become unidentifiable, and
759   different parameter values corresponding to different introgression histories can explain the data
760   equally well. For each of the two inversion regions, we found distinct peaks in the posterior
761   distribution which correspond to different historical scenarios with opposite introgression directions
762   between (*H. sara, H. demeter*) and *H. telesiphe* (**Fig. 6**). Both scenarios are consistent with the
763   known inversion orientations in modern species. Here, we discuss evidence in favour of each
764   introgression scenario, although it is difficult to rule out alternatives.

765   In the chromosome 2b region (1.95 Mb, with 411 noncoding loci and 516 coding loci), introgression
766   between the common ancestor of the *sara* clade and *H. telesiphe* was inferred to be unidirectional
767   with $1 - \varphi_{tc2} \approx 0.9$ and $1 - \varphi_{ds2} \approx 0$ in scenario 1 (**Fig. 6a**), while in scenario 2, introgression was
768   mostly unidirectional but in the opposite direction ($1 - \varphi_{tc2} \approx 0$, $1 - \varphi_{ds2} \approx 0.8$). Both scenarios are
769   consistent with tree iii (**Fig. 2**), where *H. telesiphe* clusters with the *sara* clade and the *H. telesiphe* →
770   *H. hecalesia* introgression was absent ($1 - \varphi_c \approx 0$). The two scenarios make similar predictions about
771   the gene-tree histories and the genetic data (for example, both scenarios predict the origin of the
772   inversion in the branch ehc), but the effective root of the species tree for the 2b region is at node r
773   in scenario 1 and at node ehtc in scenario 2.

774   To determine which scenario is more consistent with other autosomal regions of the genome, we
775   compared the root age of the inversion region with τ_r and τ_{ehtc} on other chromosomes. Divergence
776   times (τ) for the 2b region are highly similar to those in other regions of the genome, with regression
777   slopes ~1.01–1.08 for the noncoding loci (**Fig. S10**), suggesting that the 2b region has a neutral
778   mutation rate similar to that of other genomic regions. Scenario 1 is supported if the root age (τ_r in
779   scenario 1, τ_{ehtc} in scenario 2) for inversion 2b is close to τ_r in other regions, while scenario 2 is
780   supported if it is closer to τ_{ehtc} from the rest of the genome. For noncoding loci, the root age of 2b
781   (posterior mean 0.026) was closer to the root age of the rest of the genome expected under scenario
782   1 (τ_r = 0.026–0.029) than that for scenario 2 (τ_{ehtc} = 0.018–0.023, **Fig. S3**, **Table S9**). Although we do

20

783   not know whether *H. telesiphe* has the inversion, its ancestor likely had the inversion, but
784   introgression from the ancestor of *H. demeter* and *H. sara* (which lack the inversion) under scenario
785   1 almost certainly caused replacement without recombination. We therefore predict that *H.*
786   *telesiphe* does not today carry the inversion, but that its ancestor did. In contrast, scenario 2 predicts
787   that *H. telesiphe* always lacked the inversion, but it would be unclear why the non-inverted region
788   from *H. telesiphe* replaced the original non-inverted sequence in the *H. demeter/H. sara* ancestor
789   with an almost complete lack of recombination. Thus, this secondary evidence also supports
790   scenario 1 (**Fig. 6a**).

791   An alternative to an introgression hypothesis requires ancestral polymorphism of the 2b inversion,
792   where *H. sara*, *H. demeter* and *H. telesiphe* retained the ancestral non-inverted orientation through
793   incomplete lineage sorting after divergence of the *erato* and *sara* clades (Edelman et al. 2019).
794   Compared with the introgression scenario, ancestral inversion polymorphism predicts that the
795   divergence time τ_{tc2} for the common ancestor of *H. telesiphe*, *H. sara* and *H. demeter* must pre-date
796   or overlap the divergence time of the entire clade found for the rest of the genome. Our results did
797   not support this hypothesis. Estimated τ_{tc2} in the 2b region (for noncoding regions, 0.018) was
798   always much closer to the introgression time in the rest of the genome ($\tau_{tc2} = 0.016-0.022$) than to
799   the root in the rest of the genome ($\tau_r = 0.026-0.029$) (**Fig. S3**, **Table S9**), suggesting that the
800   introgression hypothesis is more likely than the inversion polymorphism hypothesis in the ancestral
801   population prior to the divergence of the entire *erato-sara* clade.

802   Based on pairwise sequence distances (D_{XY}), Edelman et al. (2019) argued that ancestral inversion
803   polymorphism could explain the data as well as or better than (*H. sara*, *H. demeter*) → *H. telesiphe*
804   introgression for inversion 2b (their Fig. S95). The introgression scenario was rejected because the
805   *H. sara*–*H. telesiphe* divergence of 2b was not much lower than the genome-wide average.
806   However, this conclusion assumes that that all other chromosomes were free of such introgression.
807   The prevalence of BDI between (*H. sara*, *H. demeter*) and *H. telesiphe* across the genome, as
808   suggested by our results (**Figs. 4b, 5**), could explain the patterns of D_{XY} in Edelman et al. (2019). The
809   possibility of the opposite introgression with *H. telesiphe* as the source species (scenario 2 in **Fig. 6a**)
810   was also not considered by Edelman et al. (2019).

811   For the chromosome 15b inversion region (580 kb, with only 149 noncoding loci and 167 coding
812   loci), two sets of estimates were always obtained from independent MCMC runs, each occurring
813   about 50% of the time. This inversion contains the *cortex* gene known to be involved in mimicry in
814   the *H. melpomene*/silvaniform group as well as the *H. erato/sara* group of *Heliconius* (Nadeau et al.
815   2016), although the precise role of the inversion in mimicry is unknown for the species studied here
816   (Edelman et al. 2019). As for the 2b region, a pair of scenarios correspond to alternative histories
817   differing in direction of introgression between the common ancestor of the *sara* clade and *H.*
818   *telesiphe* (**Fig. 6b**). Again, both scenarios are consistent with the pattern of shared derived
819   orientation of the inversion region among *H. telesiphe*, *H. hecalesia*, *H. demeter* and *H. sara*, as
820   represented by tree iv (**Fig. 2**). In both scenarios, the inversion originated along the branch between
821   the root and the introgression between the ancestral populations of *H. telesiphe* and *H. demeter/H.*
822   *sara* (**Fig. 6b**). As before, we used the root age (τ_r under scenario 1 and τ_{ehtc} under scenario 2) to
823   distinguish between these two possibilities. Note that the divergence time estimates in the 15b
824   region are also highly comparable to those in other genomic regions, with regression slopes ~1.00–
825   1.07 for the noncoding loci (**Fig. S11**). The comparison suggests that introgression from the common
826   ancestor of *H. sara* and *H. demeter* into the ancestor of *H. telesiphe* was more compatible with the
827   other regions of the genome than the opposite direction (**Fig. S3**, **Table S9**), even though the
828   opposite direction of introgression was marginally more prevalent across the rest of the genome
829   (**Fig. 5**). Our result for 15b is concordant with the findings of Edelman et al. (2019), who used
830   internal branch lengths and D_{XY} to suggest introgression as a likely scenario, although they did not
831   consider the alternative scenario 2 of introgression (**Fig. 6b**).

832   Our results provide evidence that introgression according to scenario 1 (**Fig. 6**) between (*H. sara, H.*
833   *demeter*) and *H. telesiphe* rather than ancestral polymorphism is a more likely explanation for the
834   history of both 2b and 15b inversion regions, and that the introgression was almost wholly
835   unidirectional. Additional genomes with inversion status from diverse species from this *erato-sara*
836   clade and better breakpoint characterization will be useful to test these conclusions about the
837   alternative scenarios.

838

839
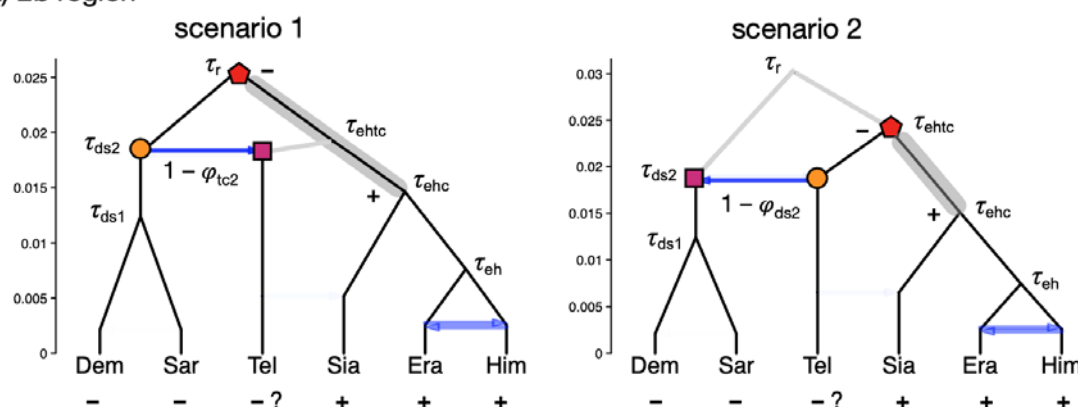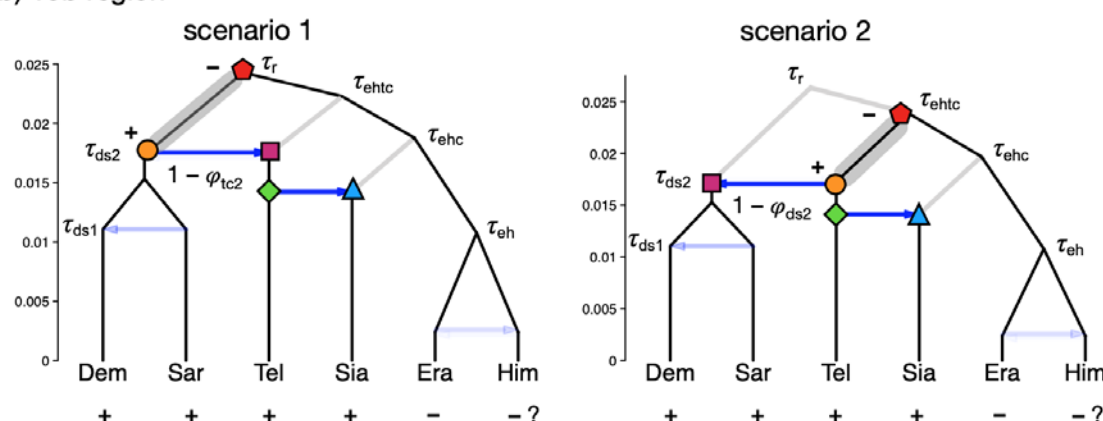
840   **Figure 6.** Within-model unidentifiability and possible introgression histories for inversion regions (**a**)
841   2b and (**b**) 15b, showing estimated divergence times from BPP analysis under the MSci model (**Fig.**
842   **4a**). For each region, there are two competing scenarios of the introgression history that fit the data
843   equally well, resulting in unidentifiability of certain model parameters. Plus (+) represents the
844   derived inverted orientation while minus (−) is the ancestral non-inverted orientation. Species with
845   uncertain inversion orientation are marked with '?'. Node symbols and colours indicate matching
846   nodes and times between the two scenarios. The estimates were based on posterior means from
847   noncoding loci. Grey band indicates an ancestral population within which the derived inverted
848   orientation (+) may have arisen from the non-inverted orientation (−). Note that parameters
849   associated with nodes reached by very few sequences (indicated as grey branches) were expected to
850   be poorly estimated, with a wide posterior interval. For example, in scenario 1 for 2b, τ_{ehtc}, θ_{ehtc} and
851   θ_{ehc} were poorly estimated (**Fig. S3**, **Table S9**).

852

853   *Evidence of introgression from natural populations*

854   Our analyses support three introgression events (**Fig. 4**): (1) between *H. telesiphe* and the common
855   ancestor of the *sara* clade, (2) from *H. telesiphe* into *H. hecalesia*, and (3) between *H. erato* and *H.*
856   *himera*. The first two are consistent with previous genomic studies (Edelman et al. 2019; Kozak et al.
857   2021). Ancient introgression such as (1) will be difficult to confirm using evidence from natural
858   populations today. The recent introgression (3) is well-documented in natural populations and in
859   mating experiments (Jiggins et al. 1997; Mcmillan et al. 1997; Mallet et al. 2007).

860   However, the six species included in this study constitute but a fraction of the species and
861   geographic races in the *erato-sara* clade, so caution should be exercised in interpretation of inferred
862   introgression. In particular, signals of introgression may be indirect, involving related species or
863   subspecies unsampled in the data.

864   For example, the *H. telesiphe* → *H. hecalesia* introgression inferred from our data may not represent
865   direct gene flow between the two species, which do not currently overlap geographically (Rosser et
866   al. 2012).   *H. hecalesia* does overlap with *H. clysonymus* and its sister species *H. hortense* in West
867   Ecuador, the Colombian Andes, and Central America (Rosser et al. 2012), and there are documented
868   natural hybrids between *H. hecalesia* and both *H. clysonymus* and *H. hortense* (Mallet et al. 2007).
869   Furthermore, *H. telesiphe* forms a well-supported clade with *H. clysonymus* and *H. hortense*, nested
870   within the *erato* clade (Kozak et al. 2015; Massardo et al. 2020; Kozak et al. 2021). Therefore, it is
871   likely that introgressed loci in *H. hecalesia* actually came from *H. clysonymus*, *H. hortense*, or their
872   common ancestor. Introgression from *H. clysonymus* or *H. hortense* is also supported by
873   phylogenetic network analysis and *D* statistics in Kozak et al. (2021).

874   Another case is the possible indirect gene flow between *H. erato* and *H. himera*. *H. himera* is
875   considered an incipient species within *H. erato* (*sensu lato*). It is restricted to middle elevations
876   (800–2,000 metres) of the Andes in South America; in contrast, the subspecies of *H. erato*
877   characterized here, *H. erato demophoon*, is found in Central America (Rosser et al. 2012). However,
878   *H. himera* is parapatric with several subspecies of *H. erato* (such as *cyrbia*, *favorinus*, *lativitta* and
879   *emma*) (Mallet 1993; Rosser et al. 2012), with narrow contact zones where natural hybrids can be
880   found at frequencies of 5–10% (Jiggins et al. 1996; Jiggins et al. 1997; Mallet et al. 1998). The recent
881   introgression signal we detect here almost certainly resulted from these adjacent subspecies of *H.*
882   *erato* rather than from *H. erato demophoon*.

883

884   *Conclusion*

885   The coalescent-based full-likelihood approach employed here was able not only to detect gene flow
886   among species, but also to estimate its direction, timing and magnitude using genomic data. We
887   have demonstrated that a much fuller understanding of the demographic and introgression history
888   of a well-studied group of species can be gained by such an approach than with methods more
889   usually employed hitherto. In the *Heliconius erato-sara* clade of species, we found robust evidence
890   of introgression across the genome involving distantly related species deep in the phylogeny as well
891   as between sister species in shallower parts of the tree. We confirm ancestral gene flow between
892   the *sara* clade and an ancestor of *H. telesiphe*, infer a likely hybrid speciation origin of *H. hecalesia*,
893   as well as gene flow between the sister species *H. erato* and *H. himera*. We clarify how introgression
894   among ancestral species can explain the history of two chromosomal inversions deep in the
895   phylogeny of the *erato-sara* group. Importantly, we estimate key population parameters such as
896   species divergence times and population sizes for modern and ancestral species of this *Heliconius*
897   clade, providing an opportunity to understand the speciation and introgression history of this group
898   in fine detail.

899

COMPETING INTEREST STATEMENT

901   The authors declare no competing interests.

902

SUPPLEMENTARY MATERIAL

904   Supplementary materials are available in Zenodo at https://doi.org/10.5281/zenodo.5639614. The
905   multilocus sequence datasets for BPP and 3s analyses are available in Dryad at
906   https://doi.org/10.5061/dryad.dfn2z3526. The C program for calculating the genotyping error rate
907   given the base-calling error and read depth is at https://github.com/abacus-gene/genotypecall. All
908   code used to filter the data are available at
909   https://github.com/fernandoseixas/EratoCladePhylogeny.

910

ACKNOWLEDGEMENTS

FUNDING

REFERENCES

924

925